Damage characterization in fiber reinforced polymer via Digital Volume Correlation

Ana Vrgoč, Zvonimir Tomičević, Benjamin Smaniotto, François Hild

Damage characterization in fiber reinforced polymer via Digital Volume Correlation

Ana Vrgoč[1], Zvonimir Tomičević[1*], Benjamin Smaniotto[2] and François Hild[2]

[1]*Laboratory of Experimental Mechanics, Faculty of Mechanical Engineering and Naval Architecture, University of Zagreb, Ivana Lučića 5, 10002, Zagreb, Croatia*
[2]*Université Paris-Saclay, ENS Paris-Saclay, CNRS, LMT – Laboratoire de Mecanique et Technologie 91190 Gif-sur-Yvette, France*

(Received keep as blank , Revised keep as blank , Accepted keep as blank)

Abstract. An *in situ* experiment imaged via X-ray computed tomography was performed on a continuous glass fiber mat reinforced epoxy resin composite. The investigated dogbone specimen was subjected to uniaxial cyclic tension. The reconstructed scans (*i.e.*, gray level volumes) were registered via Digital Volume Correlation. The calculated maximum principal strain fields and correlation residual maps exhibited strain localization areas within the material bulk, thus indicating damage inception and growth toward the specimen surface. Strained bands and areas of elevated correlation residuals were mainly concentrated in the narrowest gauge section of the investigated specimen, as well as on the specimen ligament edges. Gray level residuals were laid over the corresponding mesostructure to highlight and characterize damage development within the material bulk.

Keywords: fiber reinforced polymer; X-ray computed tomography; Digital volume correlation; damage; correlation residuals

1. Introduction

X-ray computed tomography (XCT) has been emerging as a powerful tool in experimental mechanics as it allows microstructural changes to be imaged in the material bulk during mechanical experiments (Maire, E. *et al*. 2014, Gigliotti, M. *et al*. 2018, Buljac, A. *et al*. 2018b). Combined with Digital Volume Correlation (DVC), such observations enable *in situ* bulk kinematic fields to be measured (Bay, B. 2008, Roux, S. *et al*. 2008, Buljac, A. *et al*. 2018b, Gigliotti, M. *et al*., 2018). Further, global approaches to DVC based on the finite element method (FEM) were introduced to register and analyze 3D volumes (Réthoré, J. *et al*. 2008, Roux, S. *et al*. 2008). Opposed to local approaches, FE-based DVC assumes the continuity of displacement fields, and of the key advantages of such approaches is the availability of correlation residual fields. The latter correspond to the gray level difference between the reference volume and the volume of the deformed material corrected by the measured displacement field. These residuals, which are probed for all voxels belonging to the inspected region, provide useful information when checking the convergence of DVC analyses (as the displacement fields are assumed to be continuous). In addition, the regions exhibiting

* Corresponding author, Assistant Professor Zvonimir Tomičević, PhD, E-mail: zvonimir.tomicevic@fsb.hr

elevated residual values for converged displacement fields unveil discontinuities, *i.e.*, the damaged zones. The analysis of correlation residual fields has proven to be successful in providing meaningful information to detect damage occurrence within material bulk (Tomičević, Z. *et al*. 2016, Tomičević, Z. *et al*. 2019, Vrgoč, A. *et al*. 2021). This is particularly crucial for assessing the bulk behavior and revealing damage processes in fiber reinforced polymers (FRP) as the heterogeneous nature of such materials induces damage at various scales (Brunner, A. 2018, Fayyadh, M. 2021, Nguyen, V.D. *et al*. 2019, Vrgoč, A. *et al*. 2021). Therefore, investigating kinematic and microstructural changes in FRPs under various loading regimes enriches the development of constitutive laws and the investigation of damage mechanisms. In the context of industrial applications, coupling XCT and DVC into a unique framework enables for the optimization of manufacturing processes and component shape, as well as in-service performances of structural parts (Naresh, K. *et al*. 2020).

The tomography experiment reported herein was performed on a dogbone sample made of continuous glass fiber mat reinforced epoxy resin and subjected to *in situ* cyclic tensile loading. Prior to loading, two scans were acquired in the undeformed configuration to quantify measurement uncertainties. The reconstructed scans were then registered via global DVC. Based on the measured bulk displacements, maximum principal strain fields were calculated and analyzed to track localization phenomena. The gray level correlation residual maps were laid over the corresponding mesostructure to observe damaged zones. Furthermore, mesostructure sections of the deformed volumes corrected by the measured displacement were analyzed, which enabled the precise identification of damage mechanisms occurring within the investigated material.

2. Experimental procedure

In the present section, the experimental protocol employed in this work is introduced. First, the manufacturing process and properties of the material studied herein are discussed. The experimental data were the applied force measured by the load cell of the *in situ* testing machine and the CT scans acquired during the cyclic tensile experiment. Finally, a brief overview of the employed DVC protocol is presented, followed by the analysis of measurement uncertainties.

2.1 Material

The material of the dogbone specimen shown in Fig. 1(a) is an epoxy resin reinforced with a continuous glass fiber mat. The laminate comprising 12 plies was produced by hand lay-up after which compression molding was performed. Moreover, the volume fractions of constituents were determined by applying gray level threshold on the micrographs of composite cross-sections obtained by optical microscopy (Vrgoč, A. *et al.* 2021.). In addition, the volume fraction of R-glass fibers was found to be 40%, while the average diameter of a single fiber inside the yarn was 9 μm. Further, the volume fraction of the matrix was equal to 55%, and since vacuum was not applied during molding, the volume fraction of air voids was found to be 5%. Orthoslices of the reference volume revealing the underlying mesostructure are shown in Fig. 1(b).

The investigated dogbone specimen was cut from a 5.8 mm thick composite plate, and thinned in the central part with a radius of 39 mm to ensure it broke in the ligament area (Fig. 1(a)). In addition, the width at the narrowest gauge section was 6 mm.

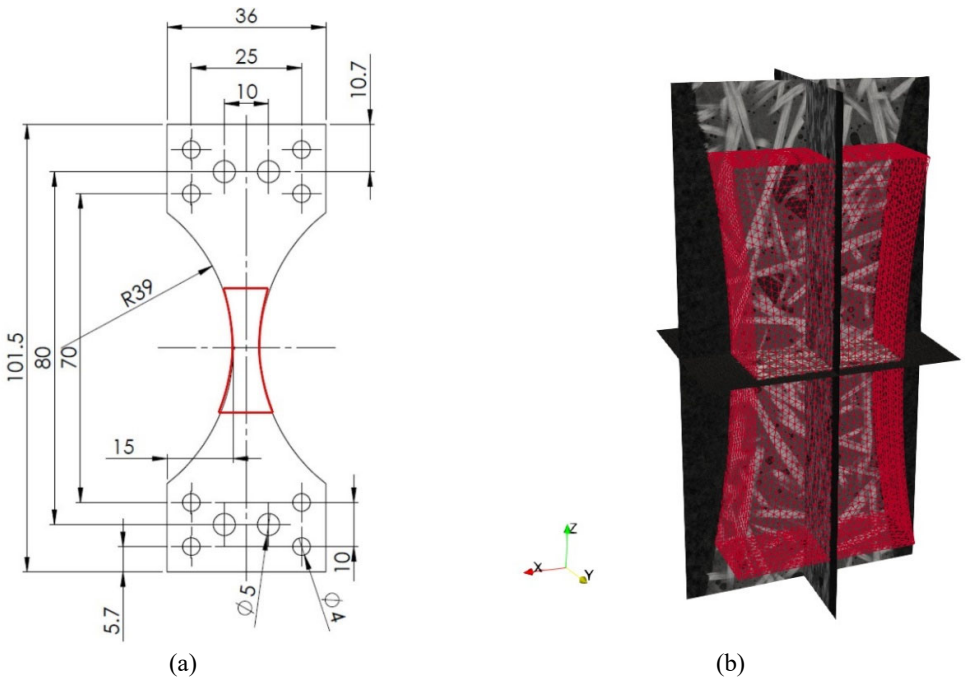

Fig. 1 (a) Geometry of the investigated dogbone specimen. The red contour depicts the region of interest. (b) Orthoslices of the reference volume revealing the underlying random mesostructure together with first-order tetrahedral mesh employed in DVC analyses. The size of the region of interest equals 610 × 410 × 1180 vx, while the physical length of one voxel is 14.6 µm.

2.2 In situ cyclic test

The studied dogbone specimen was subjected to cyclic tension with the *in situ* TTC Deben testing machine in the X50+ scanner (North Star Imaging) of LMT. The test was composed of 3 loading cycles corresponding to 30%, 60% and 90% of the ultimate tensile strength (σ_m = 120 MPa). The specimen was loaded in a displacement-controlled mode with a prescribed stroke rate of 3 µm/s. The 10 scans were acquired in loaded and unloaded configurations (*i.e.,* after applying each loading step, Fig. 2). The first acquisition (scan 0) was performed with high quality (HQ) parameters (Table 1), which resulted in low noise levels. This scan was considered as the reference scan for assessing the measurement uncertainties and performing subsequent correlations. However, the entire reference scan required approximately 2 hours to be completed. Changing the number of averaging frames to 1 for low quality (LQ) scans resulted in 4 min acquisitions. The LQ scanning parameters were employed for all subsequent acquisitions (scans 00-07) to reduce the time of the mechanical test. The second scan (00) was performed in the pre-loaded state (*i.e.*, F=400 N). At the end of the *in situ* test, a final *post mortem* HQ scan was performed (scan 7).

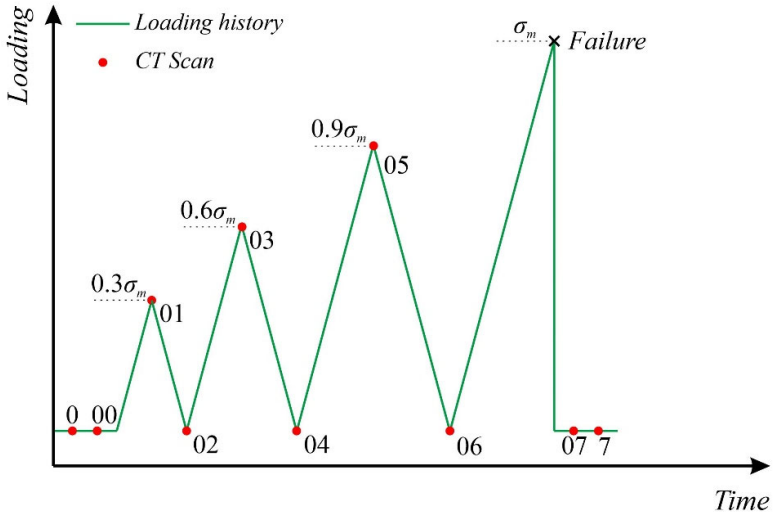

Fig. 2 Schematic representation of the loading history for the *in situ* cyclic tensile test. The red solid circles denote the positions at which a new scan was acquired. The first two acquisitions were performed in the undeformed state to quantify measurement uncertainties.

A filtered-back projection algorithm (Kak, A., Stanley, M. 1998) was utilized to reconstruct 3D volumes from a series of acquired radiographs. The reconstructed volumes represent the scanned region whose size was initially equal to 1507 × 1507 × 1849 vx encoded as 8-bit deep gray levels. The physical size of one voxel was found to be 14.6 µm. Since conducting volumetric correlations with the full-size reconstructed volumes was computationally too demanding, only a part of the reconstructed volume was considered herein. The region of interest (ROI) tailored to the actual specimen geometry and focusing on the central (*i.e.*, thinned) part had a size of 499 × 685 × 1401 vx (Fig. 1). Table 1 summarizes the scanning parameters.

Table 1 Scanning parameters

Tomograph	North Star Imaging X50+	
X-ray source	XRayWorX XWT-240-CT	
Target / Anode	W (reflection mode)	
Filter	None	
Voltage	145 kV	
Current	78 µA	
Focal spot size	5 µm	
Tube to detector	910 mm	
Tube to object	53 mm	
Detector	Dexela 2922	
Definition	1507 x 1849 px (2 × 2 binning)	
Scanning parameters	High quality (HQ)	Low quality (LQ)
Number of projections	800	768
Angular amplitude	360°	360°
Frame average	20 per projection	Continuous (1 per projection)
Frame rate	3 fps	3 fps
Acquisition duration	1 h 46 min 26 s	4 min 26 s
Reconstruction algorithm	Filtered back-projection	Filtered back-projection
Gray levels amplitude	8 bits	8 bits
Volume size	499 × 685 × 1401 vx (after crop)	499 × 685 × 1401 vx (after crop)
Field of view	7.3 × 10 × 20.5 mm^3	7.3 × 10 × 20.5 mm^3
Image scale	14.6 µm / vx	14.6 µm / vx
Pattern	Natural (Fig. 1. (b))	Natural (Fig. 1(b))

2.3. Digital Volume Correlation

DVC employed herein is the 3D extension of 2D global Digital Image Correlation (DIC) (Roux, S. *et al*. 2008, Leclerc, H. *et al*. 2015, Buljac, A. *et al*. 2018b). As each voxel within the reconstructed volume contains a gray level information determined by the absorption coefficient of X-rays, the full-field measurement technique consists in matching the gray levels between a scan in the reference *f* configuration and another one in the deformed state *g* assuming gray level conservation

$$f(\mathbf{x}) = g(\mathbf{x}+\mathbf{u}(\mathbf{x})), \tag{0.1}$$

where **x** denotes the voxel location, and **u**(**x**) the sought displacement field. The solution consists in minimizing the L2-norm of gray level residual $\varphi_C(\mathbf{x}) = f(\mathbf{x}) - g(\mathbf{x}+\mathbf{u}(\mathbf{x}))$ with respect to the kinematic unknowns related to the parametrization of the sought displacement field. In the present work, a global approach to DVC assuming continuity of the displacement field was employed. The displacement field is written as follows

$$\mathbf{u}(\mathbf{x}) = \sum_n u_n \boldsymbol{\psi}_n(\mathbf{x}), \tag{0.2}$$

where $\boldsymbol{\psi}_n$ are the shape functions associated with the finite element discretization of the displacement field, and u_n the associated nodal displacements. Thus, the global residual Φ_C

$$\Phi_C = \sum_{\mathrm{ROI}} {\varphi_C}^2(\mathbf{x}) \tag{0.3}$$

is minimized with respect to all unknown degrees of freedom u_n gathered in the displacement vector $\{\mathbf{u}\}$. In the present case, the FE discretization was based on first-order tetrahedral elements. Furthermore, a Gauss-Newton scheme is implemented to iteratively solve linear systems, and thus determine corrections to the sought nodal displacement field $\{\delta\mathbf{u}\}$

$$[\mathbf{M}]\{\delta\mathbf{u}\} = \{\mathbf{b}^i\}, \tag{0.4}$$

where $[\mathbf{M}]$ represents the DVC matrix gathering shape functions and image gradient, and which is computed only once

$$M_{nm} = \sum_{\mathrm{ROI}} \big(\nabla f(\mathbf{x}) \cdot \psi_m(\mathbf{x})\big)\big(\nabla f(\mathbf{x}) \cdot \psi_n(\mathbf{x})\big). \tag{0.5}$$

the residual vector $\{\mathbf{b}^i\}$ at iteration *i* comprises the current gray level residual, namely, the gray level difference between the reference volume *f* and the corrected deformed volume $\tilde{g}(\mathbf{x}) = g(\mathbf{x} + \mathbf{u}^i(\mathbf{x}))$

$$b_m^i = \sum_{ROI} \big(f(\mathbf{x}) - \tilde{g}^i(\mathbf{x})\big)\big(\nabla f(\mathbf{x}) \cdot \boldsymbol{\psi}_m(\mathbf{x})\big), \tag{0.6}$$

and $\mathbf{u}^i$ the current estimate of the displacement field. The convergence of the correlation algorithm is achieved when the L2 norm of the displacement vector correction $\{\delta\mathbf{u}\}$ becomes less than 10^{-3} vx.

DVC analyses may be further regularized even in low-contrast zones with additional mechanical knowledge, which is referred to as mechanical regularization based on the equilibrium gap method (Tomičević, Z. *et al*. 2013, Mendoza, A. *et al*. 2019). The latter enforces smoothness of measured fields by acting as a low-pass filter that dampens out high spatial frequencies of displacement fields. It is achieved by means of characteristic regularization lengths. When FE discretizations are employed, the regularization is activated for any length greater than the element size.

One of the major advantages of global DVC is the availability of gray level correlation residual maps, which serve as inspection tool for registration quality. If the hypothesis of gray level

conservation is not satisfied, it manifests itself in voxel-wise gray level residual increase. For instance, localized areas exhibiting elevated correlation residuals are expected to appear, indicating damage inception and growth (Mazars, V. *et al*. 2017, Buljac, A. *et al*. 2018a). It is noteworthy to highlight that in the present study the measurement of bulk kinematics between various constituents was possible due to natural contrast features (Fig. 1(b)). The regularized FE-based DVC code implemented within the *Correli 3.0* framework (Leclerc, H. *et al*. 2015) was employed to measure bulk kinematic fields. The ROI considered herein and discretized with first-order tetrahedral (T4) elements is shown in Fig. 1(b). The average element length, calculated as the cube root of the mean element volume, was 18 vx. Table 2 summarizes the parameters utilized in the DVC analyses.

Table 2 Digital Volume Correlation analysis parameters

DVC software	Correli 3.0 (Leclerc *et al*. 2015)
Image filtering	None
Mean element length	18 vx
Shape functions	Linear (T4 elements)
Mesh	Unstructured (Fig. 1(b))
Matching criterion	Penalized sum of square differences
Regularization length	Bulk: 96 vx, Dirichlet surfaces: 64 vx
Interpolant	Cubic

2.4. Displacement and strain uncertainty

Before discussing any result, the measurement uncertainties were quantified by correlating two consecutive scans acquired prior to cycling the specimen, namely, scans 0 and scan 00 (Table 3). The uncertainties were evaluated by the standard deviation of the measured displacement and calculated maximum eigen strain fields. The uncertainty values reported in Table 3 present upper bounds with the selected procedure. Let us recall that the scanning settings differed between the first two acquisitions (Table 1), and LQ settings resulted in higher noise levels. In addition, scan 00 was acquired in a pre-loaded state. Hence, slightly elevated levels of displacement uncertainties are reported, which are also related to the tomography artifacts (*i.e.*, acquisition noise, reconstruction artifacts, spurious motions during scanning (Buljac *et al*. 2018)) and natural contrast.

Table 3 Digital Volume Correlation measurement uncertainties

Displacement noise floor ($x\ y\ z$)	0.08 vx 0.06 vx 0.04 vx
Strain noise floor (ε_1)	8×10^{-5}

3. Results

The present section details the results of DVC analyses to characterize damage within the bulk of the investigated material. First, the material response of the cyclic test was determined. The first output of DVC was measured displacement fields, based on which 3D eigen strain fields were calculated. Furthermore, voxel-based maximum principal strain fields and gray level residual maps were studied to track damage development on various scales. Finally, correlation residual maps were

laid over the corresponding mesostructure to relate microstructural and kinematic changes to damage inception and growth.

3.1 DVC measurements

Figure 3 shows the mean maximum principal strain history of the experiment obtained with a virtual gauge positioned over the ligament area of the ROI, while Table 4 reports both stress and maximum eigen strain values extracted for each acquisition. The reported uniaxial stress was determined as the ratio of force by the initial cross-section area of the specimen ligament. From the reported stress–strain response, a decrease of the macroscopic stiffness is observed. As the scan 00 was performed in the preloaded state, a mean strain level of 0.002 was reported. At the peak of the first loading cycle (corresponding to 30% of the ultimate tensile strength) a mean strain level of 0.007 was found, which led to an initial Young's modulus of 9 GPa. When cycling the specimen to 60% of its ultimate tensile strength (*i.e.*, between scans 02 and 03), the corresponding Young's modulus decreased by about 30%. Unloading the specimen (scan 04) resulted in a mean strain level very close to that observed in scan 02 and 00 (*i.e.*, no permanent strain). For the last cycle prior to specimen failure (between scans 04 and 05), the Young's modulus further degraded by about 20%. In this last cycle, modest permanent strains were observed. As the decrease of Young's modulus is observed in the last loading cycle (*i.e.*, between scans 04 and 05) and modest permanent strains were reported after the third cycle (scan 06), it was concluded that damage was expected to occur within the investigated glass fiber reinforced composite.

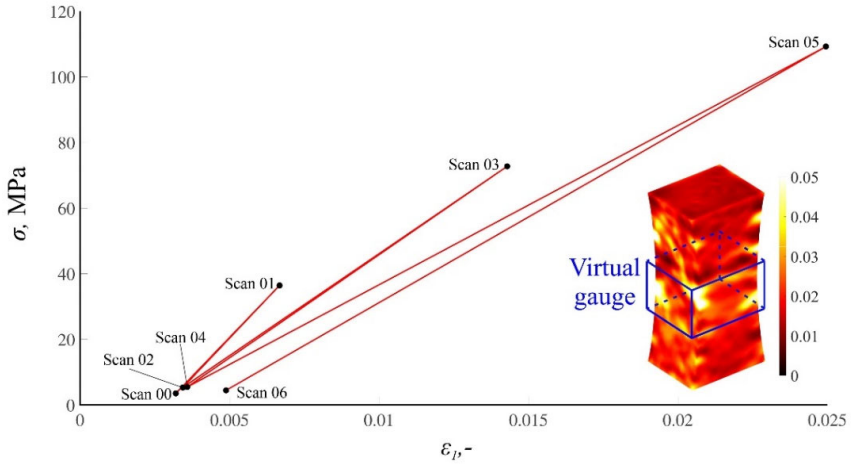

Fig. 3 Stress / strain response of the cyclic tensile experiment. The solid black circles denote the positions at which each new acquisition was performed. The blue rectangle plotted over the maximum principal strain field calculated prior to specimen failure depicts the virtual gauge utilized to calculate mean strain levels in the central part of the investigated region of interest.

Table 4 Stress and maximum eigen strain levels for different cycles of the *in situ* tensile experiment

Scan number	σ, MPa	ε_1, -
00	4	0.002
01	36	0.0067
02	5	0.0034
03	72	0.0143
04	5	0.0035
05	109	0.0250
06	5	0.0049

Figure 4 shows maximum principal strain fields and correlation residual maps for the first cycle of the *in situ* tensile experiment. The voxel-based maximum principal strain fields were thresholded such that the complex kinematics occurring within the bulk of the investigated ROI could be examined. The dynamic range of the correlation residuals was selected in a way that all estimated levels that did not lie within the absolute range from 60 to 150 gray levels originated from mechanical causes.

Figure 4(a-b) shows the initial maximum principal strain field and correlation residual map. Both fields exhibit very low values that are homogeneously distributed over the considered ROI. However, during the first loading step, maximum principal strains concentrated in a strained band in the narrowest gauge section (as the precursor to the final failure path, Fig. 4(c)). Additional areas of elevated maximum principal strains are observed on the specimen ligament edges, thereby highlighting the impact of specimen machining. The correlation residual field of scan 01 exhibited sufficiently low values within the entire ROI. This result indicates that the hypothesis of gray level conservation and continuity of the displacement field was still satisfied, hence damage growth did not yet occur or remained very limited (Fig. 4(d)). Unloading the specimen (scan 02) resulted in homogeneous and very low maximum principal strains (apart from measurement uncertainties), as well as homogeneous correlation residuals (Fig 4(e-f)).

For the subsequent loading step (*i.e.*, scan 03), the concentration of maximum principal strains in bands was more apparent, and the strain levels inside the observed bands increased (Fig. 5(a)). High levels in the residual map of scan 03 were observed within the material bulk and near the specimen front surface (Fig. 5(b)). The residuals in the remainder of the ROI were sufficiently low to prove successful convergence of DVC. The observed phenomena indicate local violation to the gray level conservation, thus indicating damage inception within the material bulk.

During the subsequent unloading step, the localized phenomena fully vanished in both maximum principal strain and correlation residual fields (Fig. 5(c-d)), *i.e.*, crack closure (or equivalently, damage deactivation) occurred. This observation exemplifies the importance of *in situ* measurements of such heterogeneous materials since unloading the specimen resulted in damage deactivation. In the last loading step prior to specimen failure, the dominant strained band, which was already detected at the beginning of the loading history, was clearly visible in the central part of the ligament (Fig. 5(e)), and multiple bands were observed along the specimen ligament edges. When studying the correlation residual field of scan 05, numerous areas of elevated residuals occurred not only in the material bulk but on the specimen surfaces as well. Some of these regions correspond to the same areas as those of scan 03 (Fig. 5(b)). The analysis of both fields proves that damage initiated in the material bulk and subsequently propagated toward the specimen surface.

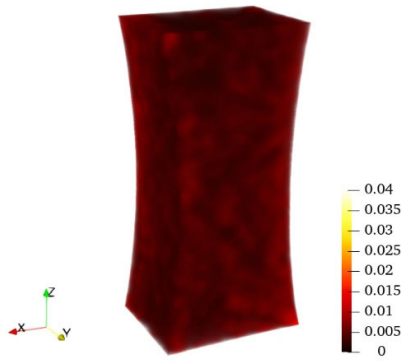

(a) ε_1 for scan 00

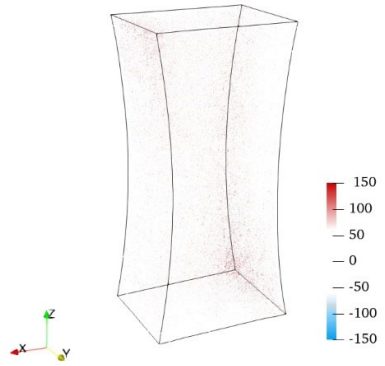

(b) φ_C for scan 00

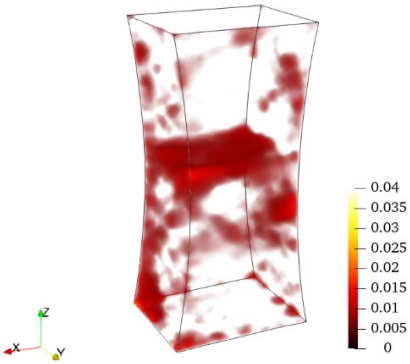

(c) ε_1 for scan 01

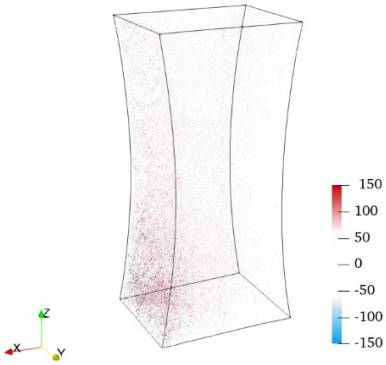

(d) φ_C for scan 01

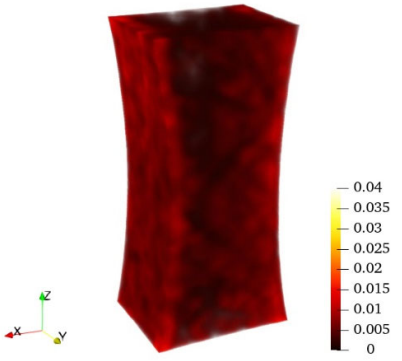

(e) ε_1 for scan 02

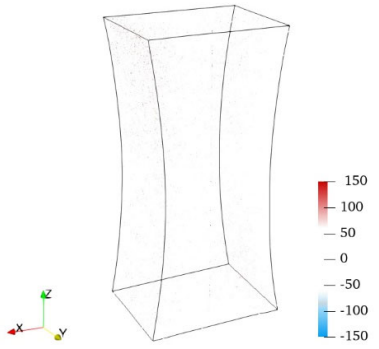

(f) φ_C for scan 02

Fig. 4 Thresholded maximum principal strain fields (left) and correlation residual maps (right) for the pre-loaded state and the first loading cycle of the *in situ* tensile experiment. The size of the region of interest corresponds to 610 × 410 × 1180 vx, while the physical length of one voxel is 14.6 µm.

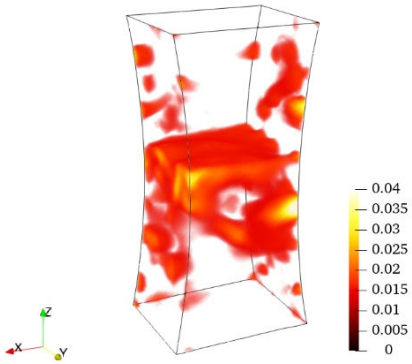

(a) ε_1 for scan 03

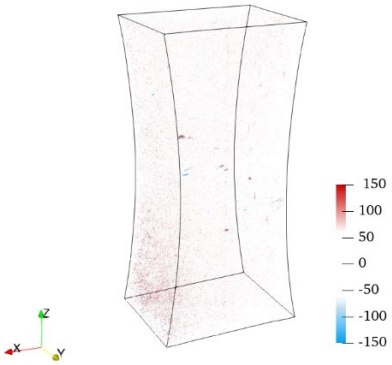

(b) φ_C for scan 03

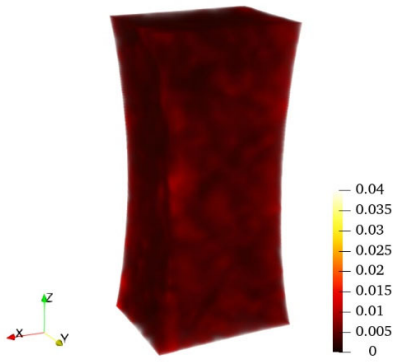

(c) ε_1 for scan 04

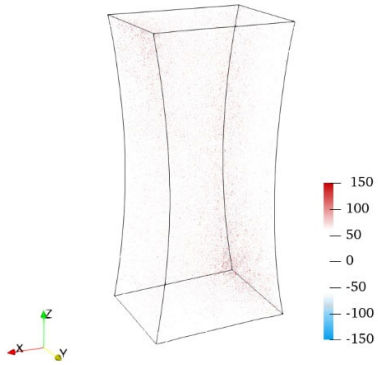

(d) φ_C for scan 04

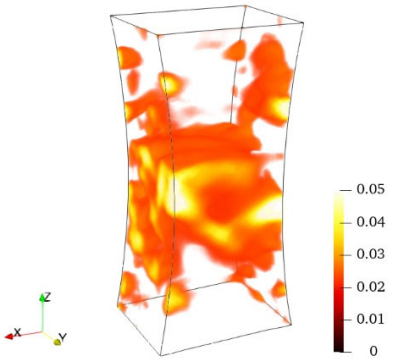

(e) ε_1 for scan 05

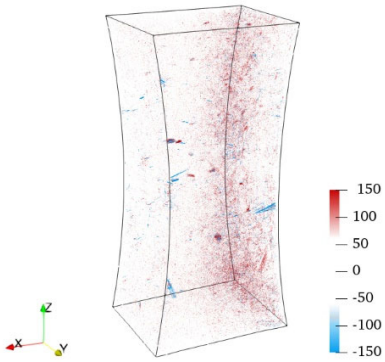

(f) φ_C for scan 05

Fig. 5 Thresholded maximum principal strain fields (left) and correlation residual maps (right) for the last two loading steps prior to specimen failure. The size of the region of interest equals to 610 × 410 × 1180 vx, while the physical length of one voxel is 14.6 µm.

3.2. Damage characterization

Damage characterization was carried out by overlaying the correlation residuals of the characteristic subregions and the corresponding mesostructure sections. In addition, mesostructure sections of the deformed volumes corrected by the measured displacement $g(\mathbf{x} + \mathbf{u}(\mathbf{x}))$ were studied in the sequel to correlate microstructural changes with measured kinematic fields. It is worth remembering that at each iteration of DVC runs, the deformed volume was corrected by the current estimate of the displacement field (Section 2.3). Consequently, the final difference between the reference and corrected volumes corresponds to the gray level residual field φ_C, which serves as an efficient tool for damage detection and characterization (Buljac, A. *et al*. 2018a).

Figure 6 shows the residual distribution of subregion 1 for scan 05, as well as the reference and corrected volumes in two perpendicular planes. The first section normal to the y-axis (y = 171 vx) was located 286 vx away from the specimen front surface having positive y-normal (y = 457 vx), while the second section was normal to the z-axis (z = 800 vx). Higher correlation residuals encompassed the fiber region passing over an air void (marked with dashed orange circles in Fig. 6). When observing the reference and corrected sections in both planes, it was concluded that the existence of air voids contributed to the damage development within the material bulk (*i.e.*, fiber breakage) as the matrix-fiber bond was degraded. It is worth recalling that the reference volume was acquired with HQ settings resulting in lower noise levels, thus the mesostructural features were imaged with sharp details. Conversely, the corrected volume was obtained from LQ scan 05, and acquisition noise is more apparent and the natural contrast between various constituents is lower compared to the HQ scan.

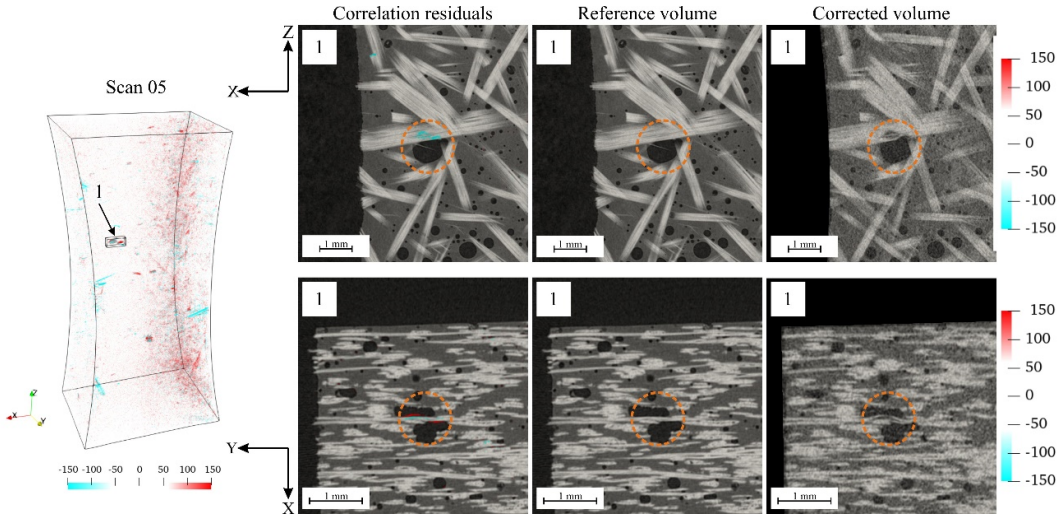

Fig. 6 Correlation residuals (scan 05) of characteristic subregion 1 laid over the corresponding mesostructure sections (first column). The second column corresponds to the reconstructed data in the reference configuration f, while the third column displays the deformed volume corrected by the measured displacement field. The dashed orange circles indicate the area of elevated correlation residuals in the two perpendicular planes.

The correlation residuals of subregion 2 were analyzed in two characteristic sections, namely, normal to the y-axis (y = 414 vx) and z-axis (z = 532 vx), see Fig. 7. Elevated correlation residuals appeared within the fiber region laying over an air void (marked with dashed orange circles). Observing the section of the corrected volume in both planes led to the conclusion that fiber breakage again occurred. The presence of air voids degraded the fiber-matrix bond, and jeopardized the integrity of the investigated specimen.

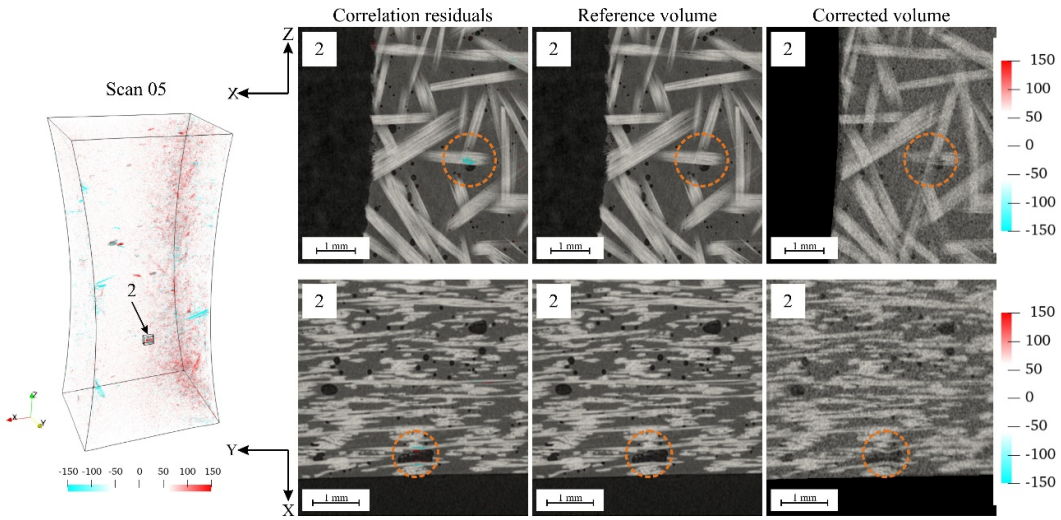

Fig. 7 Correlation residuals (scan 05) of characteristic subregion 2 laid over the corresponding mesostructure sections (first column). The second column corresponds to the reconstructed data in the reference configuration f, while the third column displays the deformed volume corrected by the measured displacement field. The dashed orange circles indicate the area of elevated correlation residuals in the two perpendicular planes.

The same procedure was followed when characterizing damage occurring in subregion 3 (Fig. 8). The first section (y = 429 vx) was located 28 vx away from the front specimen surface, whereas the second section was normal to the x-axis (x = 180 vx). In that case, the correlation residual maps of both analyzed sections laid over the corresponding mesostructure exhibited elevated levels along the longitudinal axis of fiber yarns (dashed orange circles in Fig. 8). The sections of the corrected volume revealed intra-yarn debonding. Let us recall that the specimen was cut in a composite plate, and thinned with a 39 mm radius in the central part. Intra-yarn debonding occurred on the specimen ligament edge, which is assumed to be due to machining induced damage.

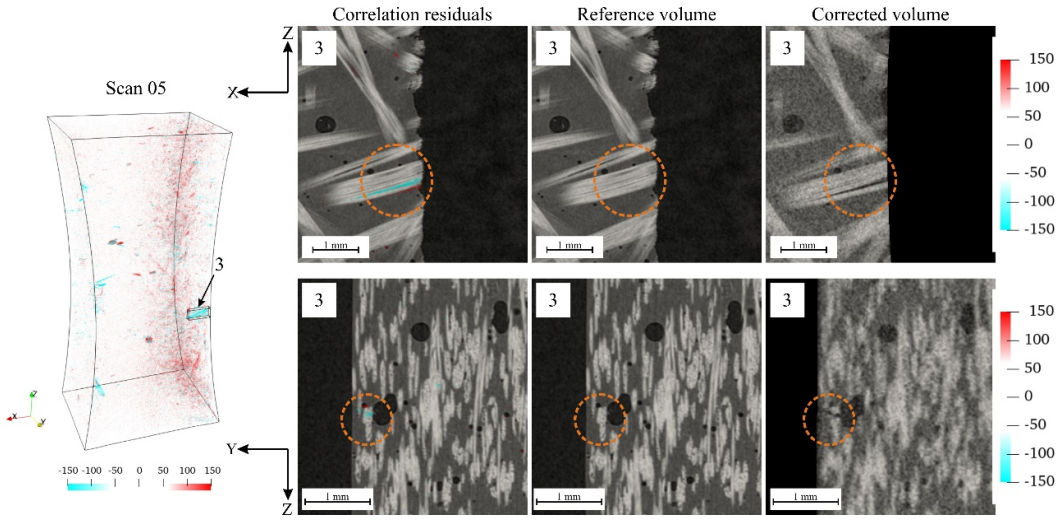

Fig. 8 Correlation residuals (scan 05) of characteristic subregion 3 laid over the corresponding mesostructure sections (first column). The second column corresponds to the reconstructed data in the reference configuration *f*, while the third column displays the deformed volume corrected by the measured displacement field. The dashed orange circles indicate the area of elevated correlation residuals in two perpendicular planes.

Intra-yarn debonding was also observed when analyzing the correlation residuals and the corrected volume sections of subregion 4 located near the specimen front surface (Fig. 9). Two perpendicular sections were investigated, the first normal to the *y*-axis ($y = 450$ vx), and the second normal to the *x*-axis ($x = 510$ vx). The correlation residual maps of both analyzed sections once again revealed elevated levels along the longitudinal direction of a fiber yarn (marked with dashed orange circles), as well as in the sections of the corrected volume. As the analyzed fiber region lied on the specimen ligament edge, this result once again exemplifies the influence of specimen machining on damage inception and growth.

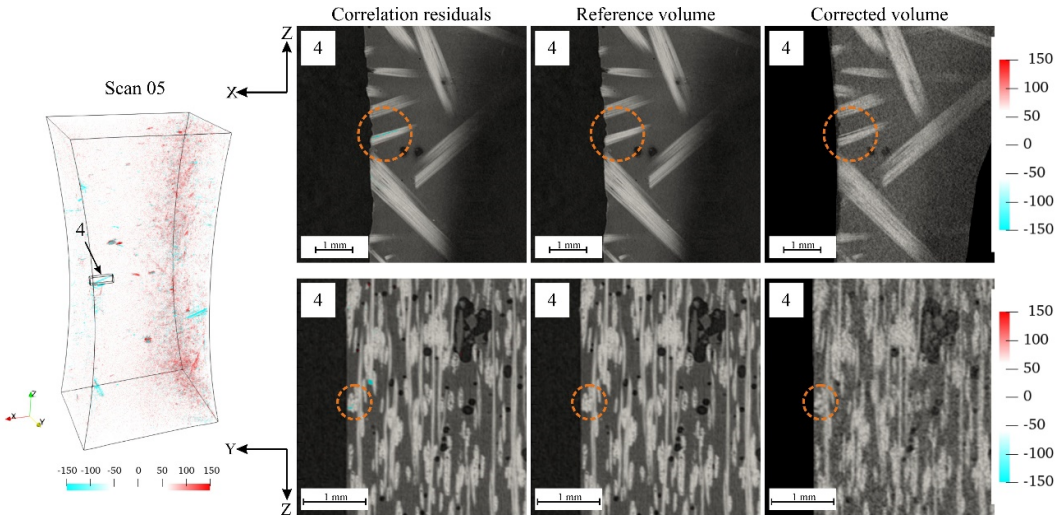

Fig. 9 Correlation residuals (scan 05) of characteristic subregion 4 laid over the corresponding mesostructure sections (first column). The second column corresponds to the reconstructed data in the reference configuration *f*, while the third column displays the deformed volume corrected by the measured displacement field. The dashed orange circles indicate the area of elevated correlation residuals in two perpendicular planes.

Figure 10 shows the correlation residual distribution of subregion 5 laid over the corresponding mesostructure. The first section ($y = 429$ vx) was located 28 vx away from the front surface, while the second section was normal to the x-axis ($x = 515$ vx). The correlation residual distributions in both sections exhibited higher levels at the end of one yarn. When observing the corrected volume sections in both planes, it was concluded that the applied load induced yarn debonding with the matrix and yarn pull-out.

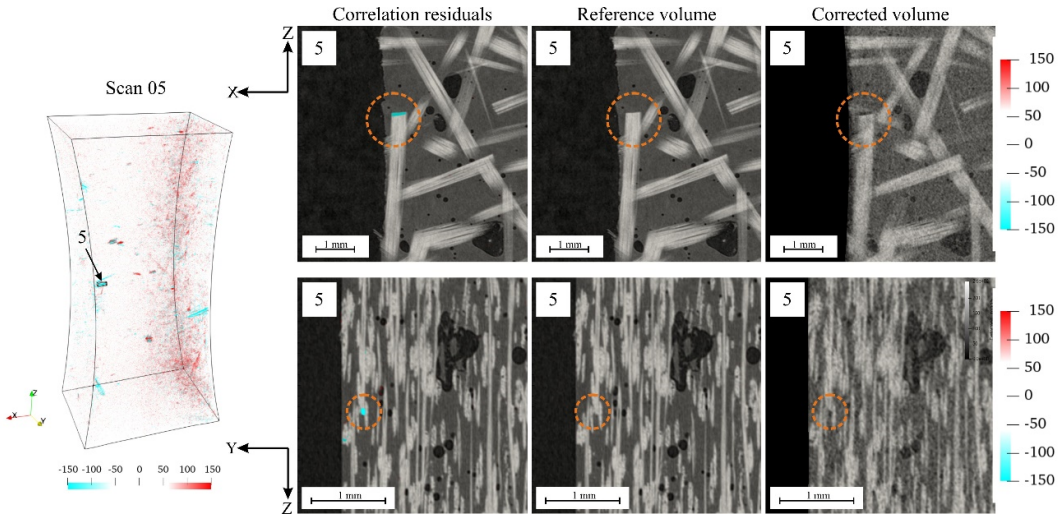

Fig.10 Correlation residuals (scan 05) of characteristic subregion 5 laid over the corresponding mesostructure sections (first column). The second column corresponds to the reconstructed data in the reference configuration *f*, while the third column displays the deformed volume corrected by the measured displacement field. The dashed orange circles indicate the area of elevated correlation residuals in two perpendicular planes.

Last, the correlation residuals of subregion 6 were analyzed in two characteristic sections, namely, for a *y*-axis normal ($y = 229$ vx) and *x*-axis normal ($x = 402$ vx), see Fig. 11. Once again, the correlation residual maps of both sections revealed yarn-end debonding and pull-out.

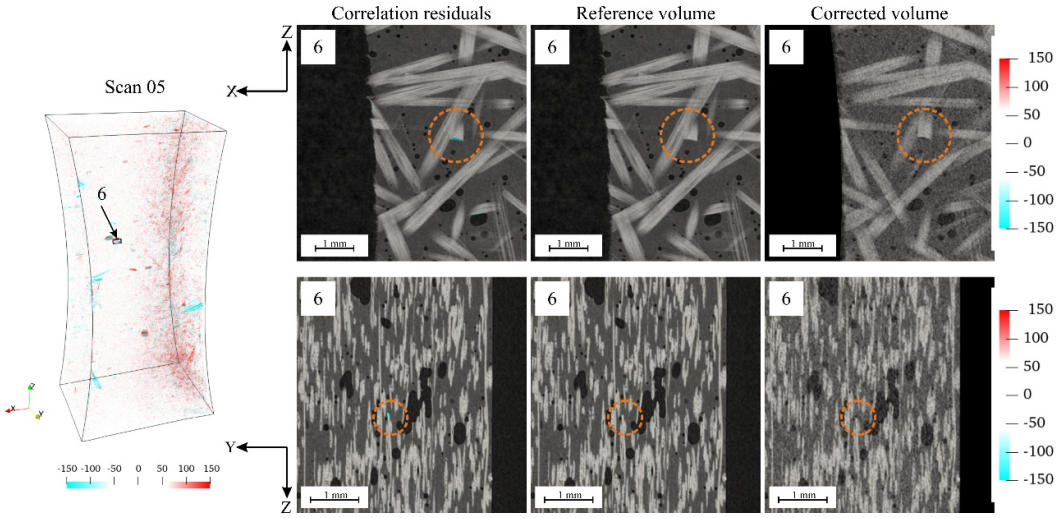

Fig.11 Correlation residuals (scan 05) of characteristic subregion 6 laid over the corresponding mesostructure sections (first column). The second column corresponds to the reconstructed data in the reference configuration *f*, while the third column displays the deformed volume corrected by the measured displacement field. The dashed orange circles indicate the area of elevated correlation residuals in two perpendicular planes.

5. Conclusions

In the reported work, an *in-situ* (tomography) experiment was performed on a continuous glass fiber mat reinforced epoxy resin. The specimen was subjected to uniaxial cyclic tension. The bulk kinematic fields were measured via FE-based DVC. The main conclusions are as follows:

- The ability of global DVC to perform measurements in the presence of strained bands encompassing the yarn architecture was demonstrated. The measurement of bulk kinematics between various constituents was possible due to the natural contrast of the studied composite. Successful DVC registrations were obtained, which was confirmed by the residual maps exhibiting sufficiently low values, except in areas where damage inception and growth occurred due to the prescribed loading (*i.e.*, areas in which the hypothesis of gray level conservation was not satisfied).
- The strained bands observed from the first loading step on were quantified in the narrowest gauge section and were mostly concentrated on the ligament edges. This observation highlighted the influence of machining on specimen integrity.
- The analysis of voxel-based maximum principal strain fields and correlation residual maps proved that damage initiated at the microscale, and subsequently propagated toward the specimen surface. The importance of *in situ* measurements for polymer composites was exemplified since observations in the unloaded configuration resulted in damage deactivation. *Ex situ* observations would have excluded the possibility of detecting the strained bands, as well as relate them to microstructural changes and damage mechanisms.

- Laying the areas of higher correlation residuals over the corresponding mesostructure sections enabled damage mechanisms to be assessed and related to mesostructural features. The analysis of correlation residual maps and corrected volume sections unveiled various damage mechanisms occurring within the bulk of the investigated specimen. The methodology employed in the present work can efficiently detect multiple microdamage mechanisms in fiber reinforced polymer composites.

Acknowledgments

This work was conducted within the FULLINSPECT project supported by the Croatian Science Foundation (UIP-2019-04-5460 Grant).

References

Abderezak, R., Daouadji, T.H., Rabia, B. (2021), "Fiber reinforced polymer in civil engineering: Shear lag effect on damaged RC cantilever beams bonded by prestressed plate", *Coupled Syst. Mech.*, **10(4)**, 299-316, https://doi.org/10.12989/csm.2021.10.4.299

Bay, B. (2008), "Methods and applications of digital volume correlation", *J. Strain Analysis*, **43**, 745-760. https://doi.org/10.1243/03093247JSA436.

Brunner, A. (2018), "Identification of damage mechanisms in fiber-reinforced polymer-matrix composites with acoustic emission and the challenge of assessing structural integrity and service-life", *Constr. Build. Mater.*, **173**, 629–37. https://doi.org/10.1016/j.conbuildmat.2018.04.084.

Buljac, A., Shakoor, M., Neggers, J., Bernacki, M., Bouchard, P., Helfen, L., Morgeneyer, T., Hild, F. (2016), "Numerical validation framework for micromechanical simulations based on synchrotron 3D imaging", *Comput. Mech.*, **59**, 419-441. https://doi.org/10.1007/s00466-016-1357-0.

Buljac, A, Helfen, L, Hild, F, Morgeneyer, T. (2018a), "Effect of void arrangement on ductile damage mechanisms in nodular graphite cast iron: In situ 3d measurements", *Eng. Fract. Mech.*, **192**, 242–61. https://doi.org/10.1016/j.engfracmech.2018.01.008.

Buljac, A., Jailin, C., Mendoza, A., Neggers, J., Taillandier-Thomas, T., Bouterf, A., Smaniotto, B., Hild, F., Roux, S. (2018b), "Digital Volume Correlation: Review of Progress and Challenges", *Exp. Mech.*, **58**, 661-708. https://doi.org/10.1007/s11340-018-0390-7.

Gigliotti, M., Pannier, Y., Gonzalez, R.A., Lafarie-Frenot, M., Lomov, S. (2018), "X-ray micro-computed-tomography characterization of cracks induced by thermal cycling in non-crimp 3D orthogonal woven composite materials with porosity", *Compos. Part A*, **112**, 100-110. https://doi.org/10.1016/j.compositesa.2018.05.020.

Kak, A., Slaney, M. (1988), "Principles of Computerized Tomographic Imaging", IEEE Press, New York, USA

Leclerc, H, Neggers, J, Mathieu, F, Hild, F, Roux, S. (2015)., "Correli 3.0.", Agence pour la Protection des Programmes, Paris (France), IDDN.FR.001.520008.000.S.P.2015.000.31500

Leclerc, H., Périé, J., Roux, S., Hild, F. (2011), "Voxel-Scale Digital Volume Correlation", *Exp. Mech.*, **51**, 479-490. https://doi.org/10.1007/S11340-010-9407-6.

Maire, E., Withers, P. (2014), "Quantitative X-ray tomography", *Int. Mater. Rev.*, **59**, 1-43. https://doi.org/10.1179/1743280413Y.0000000023.

Mazars, V., Caty, O., Couégnat, G., Bouterf, A., Roux, S., Denneulin, S., Pailhes, J., Vignoles, G. (2017), "Damage investigation and modeling of 3D woven ceramic matrix composites from X-ray tomography in-situ tensile tests", *Acta Mater.*, **140**, 130-139. https://doi.org/10.1016/10.1016/J.ACTAMAT.2017.08.034.

Mendoza, A, Neggers, J, Hild, F, Roux, S. (2019), "Complete mechanical regularization applied to digital

image and volume correlation", *Comput. Method. Appl. Mech. Eng.*, **355**, 27-43. https://doi.org/10.1016/j.cma.2019.06.005.

Naresh, K., Khan, K.A., Umer, R., Cantwell, W. (2020), "The use of X-ray computed tomography for design and process modeling of aerospace composites: A review", *Mater. Des.,* **190**, 108553. https://doi.org/10.1016/j.matdes.2020.108553.

Nguyen ,V.D., Wu, L., Noels, L. (2019), "A micro-mechanical model of reinforced polymer failure with length scale effects and predictive capabilities. validation on carbon fiber reinforced high-crosslinked rtm6 epoxy resin", *Mech. Mater.*, **133**, 193–213. https://doi.org/10.1016/j.mechmat.2019.02.017.

Réthoré, J., Tinnes, J.-P., Roux, S., Buffière, J.-Y., Hild, F. (2008), "Extended three-dimensional digital image correlation (X3D-DIC)", *Comptes Rendus Mécanique*, **336(8)**, 643-649, https://doi.org/10.1016/j.crme.2008.06.006.

Roux, S., Hild, F., Viot, P., Bernard, D. (2008), "Three dimensional image correlation from X-Ray computed tomography of solid foam", *Comp. Part A*, **39**, 1253-1265. https://doi.org/10.1016/J.COMPOSITESA.2007.11.011.

Tomičević. Z, Hild. F, Roux, S. (2013), "Mechanics-aided digital image correlation", *J. Strain Analysis*, **48**, 330-343. https://doi.org/ 10.1177/0309324713482457.

Tomičević, Z., Roux, S., Hild, F. (2016), "Evaluation of fatigue crack network growth in cast iron for different biaxial loading paths via full-field measurements", *Int J Fatigue*, **92**, 281-303, https://doi.org/10.1016/j.ijfatigue.2016.07.013

Tomičević, Z., Bouterf, A., Surma, R., Hild, F. (2019), "Damage observation in glass fiber reinforced composites via μ-tomography", *Mater Today: Proc*, **12**, 185-191, https://doi.org/10.1016/j.matpr.2019.03.093

Vrgoč, A., Tomičević, Z., Smaniotto, B., Hild, F. (2021), "Application of different imaging techniques for the characterization of damage in fiber reinforced polymer", *Comp. Part A,* **150,** https://doi.org/10.1016/j.compositesa.2021.106576.